The Journal of Chemical Physics

Delocalization effects in singlet fission: Comparing models with two and three interacting molecules

Cite as: J. Chem. Phys. **152**, 244125 (2020); https://doi.org/10.1063/5.0009914
Submitted: 04 April 2020 . Accepted: 09 June 2020 . Published Online: 29 June 2020

Davide Accomasso, Giovanni Granucci, Meilani Wibowo, and Maurizio Persico

AIP Publishing

The Journal of Chemical Physics ARTICLE scitation.org/journal/jcp

Delocalization effects in singlet fission: Comparing models with two and three interacting molecules

Cite as: J. Chem. Phys. 152, 244125 (2020); doi: 10.1063/5.0009914
Submitted: 4 April 2020 • Accepted: 9 June 2020 •
Published Online: 29 June 2020

Davide Accomasso,[1] Giovanni Granucci,[1,a)] Meilani Wibowo,[2] and Maurizio Persico[1]

AFFILIATIONS

[1] Università di Pisa, Dipartimento di Chimica e Chimica Industriale, via G. Moruzzi 13, 56124 Pisa, Italy
[2] School of Chemistry, University of Nottingham, University Park, Nottingham NG7 2RD, United Kingdom

Note: This paper is part of the JCP Special Topic on Up- and Down-Conversion in Molecules and Materials.
[a)] **Author to whom correspondence should be addressed:** giovanni.granucci@unipi.it

ABSTRACT

We present surface hopping simulations of singlet fission in 2,5-bis(fluorene-9-ylidene)-2,5-dihydrothiophene (ThBF). In particular, we performed simulations based on quantum mechanics/molecular mechanics (QM/MM) schemes in which either two or three ThBF molecules are inserted in the QM region and embedded in their MM crystal environment. Our aim was to investigate the changes in the photodynamics that are brought about by extending the delocalization of the excited states beyond the minimal model of a dimer. In the simulations based on the trimer model, compared to the dimer-based ones, we observed a faster time evolution of the state populations, with the largest differences associated with both the rise and decay times for the intermediate charge transfer states. Moreover, for the trimer, we predicted a singlet fission quantum yield of ~204%, which is larger than both the one extracted for the dimer (~179%) and the theoretical upper limit of 200% for the dimer-based model of singlet fission. Although our study cannot account for the effects of extending the delocalization beyond three molecules, our findings clearly indicate how and why the singlet fission dynamics can be affected.

I. INTRODUCTION

Singlet fission (SF) is a process whereby a singlet excited state (S^*), typically generated by absorption of one photon, is converted into two lower energy triplet excitons.[1–4] Since the two triplets, each located on one chromophore, can combine to form an overall singlet state (hereafter referred to as TT), the process is spin-allowed and hence potentially fast. In particular, it typically occurs on a sub-picosecond to picosecond timescale,[5–7] outcompeting the S^* radiative and radiationless decays to the ground state.

In recent years, SF has attracted significant attention mainly because of its possible application in photovoltaics.[8] In fact, it was shown that by exploiting SF, the energy conversion efficiency of single junction solar cells can overcome the Shockley–Queisser limit of about 1/3 and reach almost 1/2.[9,10] Additionally, in the last few years, other promising applications of SF have been identified. Specifically, the process can be utilized to enhance the exciton production efficiency in organic light-emitting diodes.[11] Furthermore, the exploitation of triplet pairs generated via SF may enable new applications in quantum information and spintronics.[12]

The SF efficiency depends on two main factors:[1–4] First, the SF process should be exothermic (but preferably only slightly so), leading to the following condition for the excitation energies of S_1 and T_1 of the individual chromophore: $\Delta E(S_1) > 2\ \Delta E(T_1)$. Moreover, the mutual placement of the chromophores is of paramount importance, affecting not only the energy levels but also the electronic couplings between the relevant states.

Different mechanisms have been so far identified to explain SF[4,13–15]: (i) the direct mechanism, which consists in the population of the TT state directly from the initial excited state S^*; (ii) the mediated one, involving higher-energy (virtual) states, generally identified to be of charge transfer (CT) character, which are hardly populated but increase the effective $S^* - TT$ coupling through the so-called superexchange effect; and (iii) the two step mechanism,

where low-lying intermediate states, possibly of CT character, are actually populated before the generation of *TT*.

Despite a significant number of investigations on a broad range of materials, most of the past theoretical and computational studies on SF have focused on the minimal model of a dimer, in which only two interacting chromophores are considered to be involved in the photophysical process.[15–21] While such a model is clearly relevant for covalent dimers, its suitability to study SF in molecular crystals is not evident and requires further investigations. Specifically, in crystals, the initial state S^* may be delocalized over more than two chromophores, as a result of the exciton coupling between monomers in their S_1 state. This effect may lead to significant changes in both the energy differences and the electronic couplings between states, which in turn may cause important variations in the SF quantum yield and transition rates. In fact, experimental and theoretical evidence show that delocalization beyond nearest neighbors and the interaction between Frenkel and charge transfer (CT) states is needed to account for the spectral features of acene crystals.[4,22,23] For instance, in TIPS-pentacene, a computational study predicted a delocalization length of 3–6 molecules at 0 K, which may shorten at room temperature.[23] Moreover, a thorough study of SF in 1,3-diphenylisobenzofurans with different crystal packings showed the inadequacy of the dimer model to interpret the experimental results.[21]

Dynamics treatments based on aggregate models beyond the dimer-based one were already applied to the study of SF.[24–27] Berkelbach *et al.*[24] applied Redfield theory to quantum mechanical (QM) models of aggregates with electron–phonon coupling and showed the importance of low-lying CT states in promoting the ultrafast SF dynamics in pentacene. Tamura *et al.*[25] employed the multiconfiguration time-dependent Hartree QM method to study the SF dynamics in trimer models of TIPS-pentacene and rubrene, showing the effect of different crystal packings. A model tailored on the properties of acene crystals showed that an extended delocalization of the excitonic states accelerates the SF dynamics,[26] while structural disorder, which decreases the delocalization, was experimentally demonstrated to have the opposite effect in acene nanoparticles[28] and films.[29] Recently, Nakano *et al.*[27] used the quantum master equation approach to investigate the photodynamics in pentacene linear aggregate models up to 20 monomers and found that the SF rate increases with the aggregate size.

While the aforementioned computational studies are based on QM treatments of selected nuclear modes, with model harmonic electronic potential energy surfaces (PESs) and couplings, here we follow a different approach: we rely on the classical trajectory (surface hopping) representation for the nuclear motion, which allows us to use realistic electronic PES and couplings, to explore the full dimensional nuclear phase space taking into account temperature effects, and to extend the simulation time to several picoseconds. In this way, we can present a more realistic and detailed account of how and why delocalization affects the SF dynamics. In particular, we present trajectory surface hopping simulations based on a quantum mechanics/molecular mechanics (QM/MM) scheme in which three interacting QM molecules of a candidate SF chromophore, namely, 2,5-bis(fluorene-9-ylidene)-2,5-dihydrothiophene (ThBF),[30] are embedded in their MM crystal environment. Subsequently, we compare the results with simulations of the same type but with only two QM molecules. ThBF was chosen because it represents a typical case where the vertical excitation energies of the dimer lie in the order $TT < S^* <$ CT and also because of our previous experience with it.[31]

This paper is organized as follows: Sections II and III introduce the QM/MM computational approach and the diabatization method employed in the simulations and in the interpretation of the results. Section IV presents the simulations based on a trimer model. The latter are then compared with the dimer-based ones in Sec. V.

II. QM/MM SIMULATION PROCEDURE

In this section, we briefly summarize the procedure we followed to construct the QM/MM crystalline clusters employed in our simulations. A similar strategy was already used and described in our previous works.[31,32]

Starting from the x-ray crystal structure determined by Kawata *et al.*,[30] an MM optimization of the atomic positions in the unit cell, using periodic boundary conditions, was performed. Then, using the MM optimized crystal structure as input geometry, we ran a molecular dynamics trajectory in the NVT ensemble, using the Berendsen thermostat algorithm.[33] In the dynamics, we used a constant temperature of 300 K, a time step of 1 fs, and a total simulation time of 10 ns. Moreover, we imposed periodic boundary conditions based on the unit cell. The crystal structure optimization and the thermal equilibration at the MM level were performed using the TINKER 6.3[34] molecular modeling package.

The last frame of the MM molecular dynamics trajectory was then used to construct the cluster for the QM/MM simulations, by replicating the single unit cell along the crystalline axes. In this way, we obtained a cluster of 490 molecules, arranged in a 7×7 array of molecular columns, each containing 10 slip-stacked molecules. In the QM/MM simulations for the trimer, three neighboring molecules in the bulk of the system were treated at the QM level, specifically the fourth, fifth, and sixth in the central slipped stack. In the case of the dimer, only the fifth and sixth molecules in the central stack were represented at the QM level. The QM subsystems are shown in Fig. 1. The other molecules of the cluster were described at the MM level.

To preserve the crystal structure during the dynamics, the coordinates of 162 MM molecules at the boundary of the cluster were kept fixed in time, while the other 328 QM and MM molecules were free to move (see Fig. 2).

In our QM/MM scheme, the QM subsystem is treated using the FOMO-CI[35] method in its complete active space variant (FOMO-CASCI), using the PM3[36] semiempirical Hamiltonian,

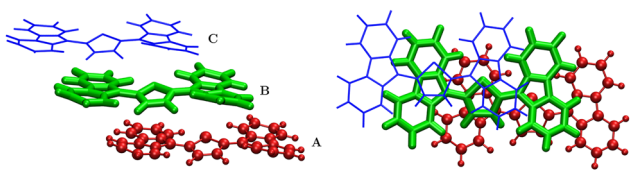

FIG. 1. QM subsystems for the simulations. Two different views are shown. In the simulations based on a trimer model, molecules *A*, *B*, and *C* are described at the QM level. In the simulations for the dimer, only molecules *A* and *B* are treated at the QM level, while molecule *C* is described at the MM level.

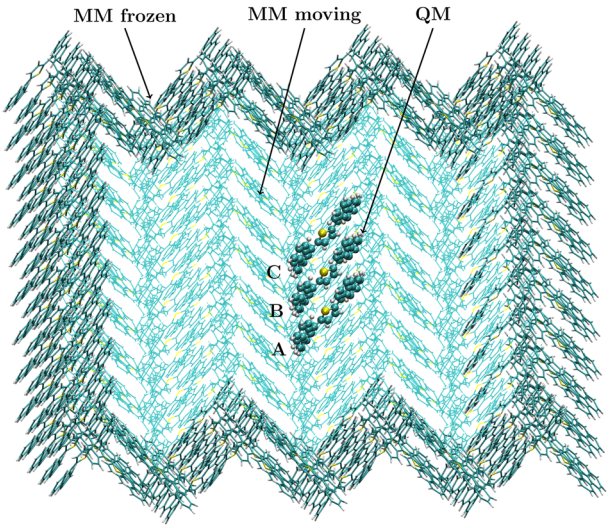

FIG. 2. A section of the QM/MM cluster employed in the simulations. In the simulations based on a trimer model, molecules *A*, *B*, and *C* are described at the QM level. In the simulations for the dimer, only molecules *A* and *B* are treated at the QM level, while molecule *C* belongs to the freely moving MM subsystem. The central trimer is represented with ball atoms and stick bonds, the molecules of the freely moving MM subsystem are shown in light colors, while the MM molecules kept frozen during the dynamics simulations are represented with thicker lines and darker colors.

reparametrized for the ThBF molecule (active space of 2 electrons in 2 orbitals), as described in Ref. 31. More details are available in supplementary material, Sec. S1. The active spaces for the dimer and the trimer were consistently chosen to be (4,4) and (6,6), respectively. In the simulations, we considered the first 12 adiabatic singlet states in energetic order for the trimer and the first 6 states for the dimer. This choice was dictated by energetic considerations and by the need to include all the states of the same nature in both simulations for a consistent comparison (see Sec. III).

Starting from the last snapshot of the thermalization MM trajectory seen above, a distribution of phase points (nuclear coordinates and velocities) was generated by performing a ground state thermal equilibration of the QM/MM system. Here, we used the Bussi–Parrinello stochastic thermostat,[37] with a constant temperature of 300 K, a time step of 0.2 fs, and a total simulation time of 14 ps.

The initial conditions (i.e., the initial electronic state, nuclear coordinates, and velocities) for the excited state trajectories were sampled from the phase space distribution generated in the last 10 ps of the ground state thermal equilibration (time interval: 4 ps–14 ps). The sampling was performed, as described in Refs. 38 and 39. In particular, excited states in a selected energy range were sampled according to their dipole transition probability.

The QM/MM simulations of the excited state dynamics were performed using a semiclassical trajectory surface hopping approach with "on the fly" calculation of adiabatic electronic energies and wavefunctions (Direct Trajectory Surface Hopping, DTSH).[35,39,40] To integrate the classical trajectories, we used a time step of 0.2 fs and a total simulation time of 4.0 ps. The overlap decoherence correction scheme[41] was used to take into account the quantum decoherence effects in a surface hopping framework. The parameters for the decoherence corrections were $\sigma = 1.0$ a.u. (Gaussian width) and $S_{min} = 0.005$ (minimum overlap). The population of the adiabatic state $\Psi_i^{(A)}$ at time t was computed as the fraction of trajectories that run on the ith adiabatic PES, i.e., the trajectories for which $\Psi_i^{(A)}$ is the current state at time t.

III. DIABATIC AND EXCITONIC STATES

To characterize the low-lying adiabatic states of the system during the simulations, we used a diabatization procedure that we recently developed and implemented in the framework of semiempirical FOMO-CASCI.[42] The procedure is based on the localization of molecular orbitals (MOs). In particular, on top of the FOMO-SCF procedure, we transform the active MOs in order to obtain orbitals that are maximally localized on one QM molecule (LMO). Then, we perform the CASCI calculation of the electronic adiabatic states using a basis of Slater determinants built on the LMOs. Finally, we determine a set of quasi-diabatic states (referred to as diabatic states from now on) by applying a unitary transformation on the adiabatic states. In our approach, the rotation matrix from the adiabatic basis to the diabatic one is defined so as to achieve maximum overlap between the diabatic wavefunctions and a set of previously chosen templates. The latter are simple wavefunctions with a well defined character, built on the LMOs.

We defined 12 diabatic states for the trimer, by means of 12 templates. The latter are the spin singlet configurations schematically illustrated in Fig. 3 (see also Sec. S2.1). In particular, they represent the ground state $S_0S_0S_0$; three singlet combinations of two triplets, TTS_0, S_0TT, and TS_0T; the localized excitations, $S_1S_0S_0$, $S_0S_1S_0$, and $S_0S_0S_1$; the singlet combination of three triplets, TTT; and the CT states $A^-B^+S_0$, $A^+B^-S_0$, $S_0B^-C^+$, and $S_0B^+C^-$, where *A*, *B*, and *C* indicate the three QM molecules. The same labels will be used to indicate both the diabatic states and their templates. The choice

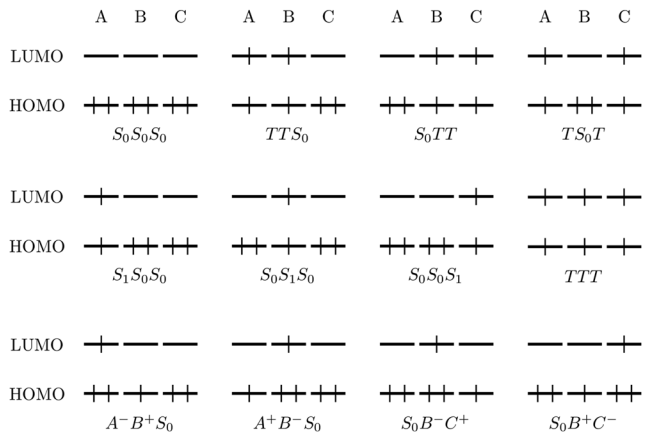

FIG. 3. Schematic representation of the 12 templates used to construct the diabatic states for a ThBF trimer. The horizontal bars indicate the LMOs, while the vertical bars stand for electrons. A, B, and C are used to label the three monomers.

of the 12 templates was based on inspection of the CI vectors for the first 12 adiabatic states and was confirmed by monitoring the projection of the CI vectors on the subspace spanned by the templates during the excited state simulations. However, we had to introduce more templates toward the end of many trajectories because of an intruder state situation encountered at geometries easily reached when the current state is of *TT* kind (see Sec. S2.4). Note that the charge transfer states involving molecules *A* and *C*, i.e., $A^-S_0C^+$ and $A^+S_0C^-$, have been excluded from this diabatic basis, mainly because they lie much higher in energy than the nearest-neighbor ones (see Table S1).

Once defined the localized diabatic basis, we found it convenient to introduce a partial delocalization by diagonalizing two blocks of the electronic Hamiltonian matrix. The two blocks correspond to the localized excitations and to the charge transfer states, and are 3 × 3 and 4 × 4 submatrices, respectively. In the new representation, the combinations of the localized excitations will be indicated as S_1^*, S_2^*, S_3^*, and the charge transfer states will be indicated as CT_1, CT_2, CT_3, CT_4 (note that within each group, S_n^* and CT_n, the states are energy ordered). In this alternative representation, the localization of excitations is lost, but the excitonic nature of the states (namely, CT vs a mixture of local excitations) is preserved: hence, it will be hereafter indicated as the excitonic basis. In this basis, the state energies are closer to the adiabatic ones that determine the nuclear trajectories. Moreover, the excitonic states are, most of the time, typical mixtures of local diabatic states with approximately fixed properties, for instance, having large or small transition dipole moments from the ground state. Therefore, the analysis of the simulation results will be conducted using the excitonic basis (see Secs. IV B and V B).

For the dimer, the diabatic states and their templates were as follows: S_0S_0, the singlet combination of two triplets indicated as *TT*; the local excitations S_1S_0, S_0S_1; and the CT states A^-B^+, A^+B^-. The excitonic basis was then obtained by diagonalizing the 2 × 2 blocks of the locally excited states and of the CT states, yielding four states named S_1^*, S_2^*, CT_1, and CT_2.

For each surface hopping trajectory, we define the population of an excitonic (or localized diabatic) state $\Psi_i^{(X)}$ as $|\langle\Psi_i^{(X)}|\Psi_k^{(A)}\rangle|^2$, where $\Psi_k^{(A)}$ is the current adiabatic state. Note that in our procedure, both the diabatic and the excitonic basis are orthonormal. We also analyzed the fluxes of populations during the simulation by computing average transition rates between pairs of excitonic states. Each transition rate is defined as the number of transitions per picosecond, divided by the number of trajectories. In the calculation of the transition rates, we considered that a transition from the excitonic (or diabatic) state *i* to *j* has occurred if, along a given trajectory, the state with the largest population (i.e., the square coefficient in the current adiabatic wavefunction) has changed from *i* to *j*. Thus, such a transition may occur either as a result of a hop between two adiabatic surfaces of different nature or because of a change in the character of the current adiabatic state along the trajectory.

IV. SIMULATIONS BASED ON A TRIMER MODEL

A. Ground state thermal equilibration

In Fig. 4, we report the energies of the excitonic states, relative to $S_0S_0S_0$, obtained during the thermal equilibration. For comparison, Figs. S1 and S2 show the excitation energies for the adiabatic

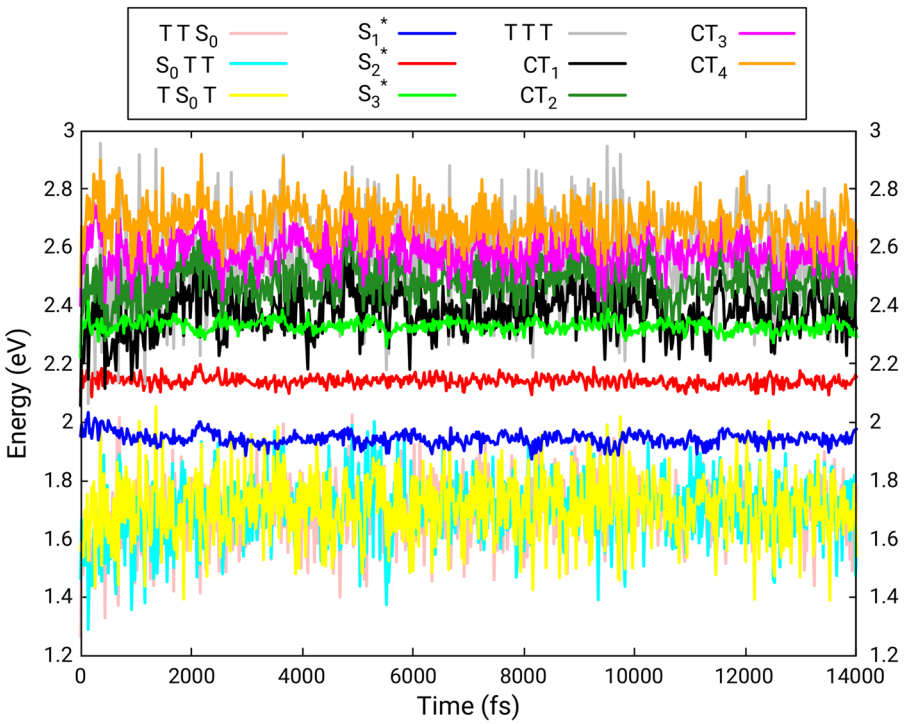

FIG. 4. Excitation energies (in eV) from the ground state ($S_0S_0S_0$) in the excitonic representation, obtained from the ground state thermal equilibration for a ThBF trimer embedded in its crystalline environment. Each point in the plot is obtained by averaging over a time interval of 20 fs.

states and for the localized diabatic ones. To distinguish the adiabatic singlet states of the three molecular systems (trimer, dimer, and monomers), hereafter we add a superscript t (S_n^t) for the trimer and a superscript d (S_n^d) for the dimer. Moreover, in Table I, we report the electronic Hamiltonian matrix in the excitonic basis, averaged over the last 10 ps of the thermal equilibration.

We see from Fig. 4 that the excitation energies of the three double triplet states, TTS_0, S_0TT, and TS_0T, oscillate around 1.7 eV, a value close to twice the vertical excitation energy of T_1 for the isolated monomer at the FOMO-CI level [$\Delta E_{vert}(T_1)$ = 0.91 eV, see Ref. 31]. The oscillations correspond to standard deviations (std) of about 0.2 eV. The TTT transition energy oscillates with std $\simeq$ 0.22 eV, around an average of 2.56 eV, close to 3/2 the energy of the double triplet states. Conversely, the transition energy fluctuations of the S_n^* states are much smaller (std $\simeq$ 0.03 eV). This difference in the bandwidths is due to the more sloped PES of T_1 with respect to S_1 in each monomer, as shown by the difference between the vertical and the adiabatic transition energies, which is 0.37 eV for T_1 and 0.01 eV for S_1.[31] The average excitation energies of the S_1^*, S_2^*, and S_3^* states are spaced by about 0.2 eV, essentially due to the first neighbor matrix elements between the localized diabatic states: $\langle S_1S_0S_0|\hat{H}_{el}|S_0S_1S_0\rangle \simeq \langle S_0S_1S_0|\hat{H}_{el}|S_0S_0S_1\rangle \simeq 0.133$ eV (see Table S2). The overall average of the three S_n^* state energies is 2.14 eV, almost exactly the vertical transition energy of the monomer: $\Delta E_{vert}(S_1)$ = 2.17 eV.[31] The transition energies of the localized charge transfer states also undergo large fluctuations (average value of about 2.5 eV, std $\simeq$ 0.15 eV), and the couplings between them are very small (see Table S2). As a result, their energies switch very frequently and each CT_n state changes its nature very often during the equilibration, but it is most of the time dominated by one localized charge transfer state. Because of the excitonic splitting of the S_n^* states, the highest of them is quasi-degenerate with the lowest charge transfer state: $\Delta E(CT_1 - S_3^*) \simeq 0.05$ in the average. The lowest one, S_1^*, lies instead close to the double triplet states: $\Delta E(S_1^* - TT) \simeq 0.23$ eV.

In Table I, we can inspect the couplings that cause transitions leading from the initially excited states to the double (or triple) triplet ones. Note that some of these matrix elements fluctuate between positive and negative values depending on molecular geometry, while others have well defined signs. We see that the couplings between the S_n^* states and two of the double triplets, TTS_0 and S_0TT, are very small (~0.10 meV), while larger matrix elements couple both kinds of states with the CT ones. Among the S_n^* excitonic states, S_1^* shows the largest electronic couplings with both the double triplet states TTS_0 and S_0TT and the charge transfer states CT_n. The "second neighbor" double triplet, TS_0T, shows non-vanishing matrix elements only with the other double triplet states and with the TTT state.

During the QM/MM thermal equilibration on the ground state, we also computed the transition dipole moments from the ground state, both in the adiabatic basis and the excitonic one (as we can see in Table II, the ground states in the two bases, S_0^t and $S_0S_0S_0$, practically coincide). The squared dipole moments, averaged over time in the interval 4 ps–14 ps, are shown in Table II for the adiabatic basis and in Table S3 for the excitonic one. Among the S_n^* states, the bright one is S_3^*, with $\langle S_0S_0S_0|\mu|S_3^*\rangle^2$ = 51.0 a.u. in the average, while S_1^* and S_2^* are essentially dark states. Among the CT_n states, the brightest is CT_1, with $\langle S_0S_0S_0|\mu|CT_1\rangle^2$ = 2.5 a.u. By making use of the adiabatic transition energies and dipoles, we computed the absorption spectrum shown in Fig. 5 as an average over the last 10 ps. The maximum of the most intense band is at 2.33 eV, in good agreement with the experimental absorption maximum at 2.30 eV in toluene solution and ~2.38 eV in a crystalline thin film.[30] Among the 11 lowest excited singlet states of the trimer, S_6^t shows the largest absorption, followed by the S_7^t, S_8^t, and S_9^t states, all other contributions to the main band being very small. As given in Table II and Table S3, this is due to the fact that the bright state S_3^* is most of the time S_6^t and more seldom the S_7^t, S_8^t, and S_9^t states, which in turn are most frequently of charge transfer type. The other two combinations resulting from exciton coupling, S_2^* and S_1^*, are most of the time the S_5^t and S_4^t states and contribute to the spectrum with the weak bands centered at about 1.95 eV and 2.15 eV, respectively. The three double triplet states, TTS_0, S_0TT, and TS_0T, are most often the low-lying excited states S_1^t, S_2^t, and S_3^t. Since the transitions from $S_0S_0S_0$ to the double triplet

TABLE I. Average electronic Hamiltonian matrix in the excitonic basis obtained from the ground state thermal equilibration of the ThBF trimer embedded in its crystalline environment. For the off-diagonal elements, if the standard deviation exceeds twice the modulus of the mean value, the former is reported with a ± sign. All matrix elements are in units of meV. Averaging time interval: 4 ps–14 ps. For more details, see Table S2, where the average Hamiltonian is also given in the diabatic basis.

$\hat{\mathscr{H}}_{el}$	$S_0S_0S_0$	TTS_0	S_0TT	TS_0T	S_1^*	S_2^*	S_3^*	TTT	CT_1	CT_2	CT_3	CT_4
$S_0S_0S_0$	0.00	±0.11	±0.09	0.00	±56.25	±57.58	±70.07	0.00	6.78	±11.29	±10.67	±8.68
TTS_0	±0.11	1703.48	0.00	±0.13	±0.12	±0.07	±0.05	±0.19	±6.86	±6.96	±7.04	±6.60
S_0TT	±0.09	0.00	1708.23	±0.12	−0.08	0.05	±0.07	±0.17	±6.85	±7.13	±7.44	±7.36
TS_0T	0.00	±0.13	±0.12	1708.41	0.00	0.00	0.00	±0.28	0.00	0.00	0.00	0.00
S_1^*	±56.25	±0.12	−0.08	0.00	1940.98	0.00	0.00	0.00	±11.77	±10.70	±11.05	±9.92
S_2^*	±57.58	±0.07	0.05	0.00	0.00	2140.65	0.00	0.00	4.94	4.90	5.08	5.42
S_3^*	±70.07	±0.05	±0.07	0.00	0.00	0.00	2327.38	0.00	±6.31	±6.09	±6.11	±5.88
TTT	0.00	±0.19	±0.17	±0.28	0.00	0.00	0.00	2563.18	0.00	0.00	0.00	0.00
CT_1	6.78	±6.86	±6.85	0.00	±11.77	4.94	±6.31	0.00	2381.33	0.00	0.00	0.00
CT_2	±11.29	±6.96	±7.13	0.00	±10.70	4.90	±6.09	0.00	0.00	2487.06	0.00	0.00
CT_3	±10.67	±7.04	±7.44	0.00	±11.05	5.08	±6.11	0.00	0.00	0.00	2582.17	0.00
CT_4	±8.68	±6.60	±7.36	0.00	±9.92	5.42	±5.88	0.00	0.00	0.00	0.00	2681.00

TABLE II. Average weights (squared coefficients) of the excitonic states in the 12 low-lying adiabatic states obtained in the thermal equilibration on S_0^t for a ThBF trimer embedded in its crystalline environment. Only weights >0.1 are reported. The relative energies (in eV) of the adiabatic states and the transition dipole moments squared (a.u.) for the adiabatic states are also reported. Averaging time interval: 4 ps–14 ps. More details in Table S3.

Adiabatic state	Most important excitonic states and their weights (in parentheses)	Energy (eV)	$\mu^2_{S_0^t \to S_n^t}$ (a.u.)
S_0^t	$S_0S_0S_0$ (0.997)	0.000	...
S_1^t	TTS_0 (0.318), S_0TT (0.324), TS_0T (0.346)	1.599	0.015
S_2^t	TTS_0 (0.366), S_0TT (0.314), TS_0T (0.269)	1.709	0.081
S_3^t	TTS_0 (0.259), S_0TT (0.293), TS_0T (0.285), S_1^* (0.159)	1.809	0.279
S_4^t	S_1^* (0.775)	1.966	1.414
S_5^t	S_2^* (0.926)	2.146	1.440
S_6^t	S_3^* (0.639), CT_1 (0.235)	2.303	35.267
S_7^t	S_3^* (0.225), CT_1 (0.651)	2.399	12.310
S_8^t	S_3^* (0.100), TTT (0.142), CT_2 (0.659)	2.478	5.458
S_9^t	TTT (0.205), CT_2 (0.301), CT_3 (0.461)	2.549	1.596
S_{10}^t	TTT (0.204), CT_3 (0.533), CT_4 (0.257)	2.623	0.201
S_{11}^t	TTT (0.257), CT_4 (0.741)	2.713	0.020

states, as well as to the dark states S_1^* and S_2^*, are dipole-forbidden, the five lowest excited states S_1^t to S_5^t do not contribute significantly to the absorption spectrum.

B. Simulation of excited state dynamics

Initial conditions (i.e., the initial electronic state, nuclear coordinates, and velocities) for 104 excited state trajectories were sampled from the phase space distribution generated in the last 10 ps of the thermal equilibration in S_0^t. In the sampling, we used a transition energy window between 2.25 eV and 2.45 eV. Consistently with the averaged transition dipole moments from S_0^t reported in Table II and with the absorption spectrum (Fig. 5), 68 trajectories started in S_6^t, 21 in S_7^t, 14 in S_8^t, and 1 in S_9^t. However, all 12 lowest singlet states of the trimer were included in the simulation.

The excitonic state populations, averaged over all trajectories, are shown in Fig. 6 as functions of time. The adiabatic and diabatic ones are in Figs. S3 and S4, respectively. The excitonic and the diabatic populations show large fluctuations, especially toward the

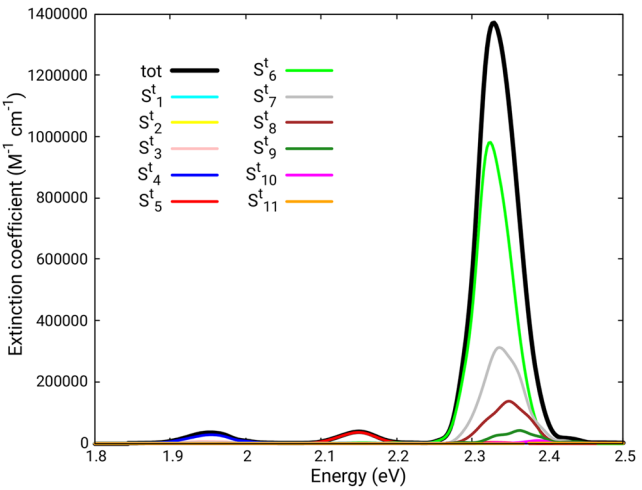

FIG. 5. Absorption spectrum obtained from the ground state thermal equilibration of a ThBF trimer embedded in its crystalline environment. Time interval: 4 ps–14 ps.

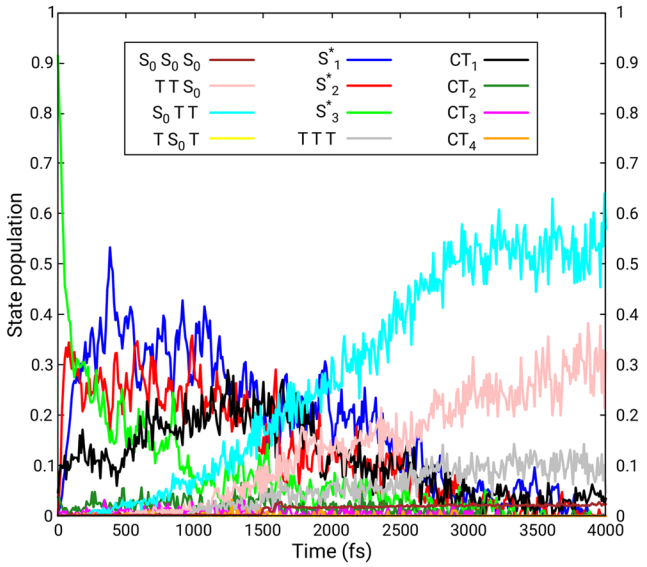

FIG. 6. State populations in the excitonic basis as functions of time for a ThBF trimer embedded in its crystalline environment. The reported results are obtained by averaging over all trajectories and time intervals of 10 fs.

end of the simulation. As shown in Sec. S2.4 of the supplementary material, such fluctuations are due to an intruder state problem and can be greatly reduced by applying a more elaborated diabatization scheme. Apart from the fluctuations, the populations obtained by the two diabatization schemes are in quite good agreement (compare Figs. S4 and S6).

In Table III, we report the average transition rates between pairs of states in the excitonic basis, along the whole simulation. To simplify the analysis, the charge transfer states, the dark excitonic states S_1^* and S_2^*, and the double triplet states are grouped together and indicated as CT, $S_{1,2}^*$, and TT, respectively, and the transitions within each group are not accounted for. The detailed state-to-state transition rates can be found in Table S5. Moreover, Fig. S5 shows the net transition rates for selected pairs of states as functions of time, in the form of histograms.

From Fig. 6 and Fig. S5, we see that the initially most populated S_3^*, corresponding to the bright combination of the localized excitations, rapidly decays to the charge transfer states CT and to the lower lying dark combinations S_2^* and S_1^*, which in turn exchange population among them (see the transition rates in Table S5). Table S6 shows that, at the initial geometries ($t = 0$), the S_3^*–CT_1 energy difference is very small (about 0.06 eV), while larger energy gaps separate S_3^* from the higher charge transfer states CT_2, CT_3, and CT_4 (about 0.15 eV, 0.24 eV, and 0.36 eV, respectively). However, all these average energy differences become very small at geometries where the $S_3^* \rightarrow CT$ transitions occur (see Table IV). The quasi-degeneracies between S_3^* and the CT states are reached mainly because of energy lowerings of the CT states in going from the starting geometries to the transition ones. Due to the fast transitions between the CT states (see Table S5), most of their population concentrates in the lowest state CT_1. In turn, the latter state transfers population to the dark state S_1^* and, to a smaller extent, to S_2^*. We see in Table IV that the $CT_1 \rightarrow S_1^*$ transitions occur when the $CT_1 - S_1^*$ energy gap is much smaller (~0.004 eV) than the one at the initial geometries (~0.446 eV), while the $\langle CT_1|\hat{\mathscr{H}}_{el}|S_1^*\rangle$ coupling remains of the same order of magnitude. This is an example among several others well documented in Table IV, showing that the accessibility of quasi-degeneracy conditions between two states, rather than the coupling strength, determines the transition rate in the presence of weak couplings. Once the S_2^* and S_1^* states are populated by transitions from both the CT and the higher lying S_3^* state, they start transferring population to the double triplet states TT and also back to S_3^* (see Table S5 and Fig. S5).

Compared to the starting geometries, at the $S_1^* \rightarrow TT$ transitions, too, we note a significant decrease in the $S_1^* - S_0TT$ and $S_1^* - TTS_0$ energy gaps (see Table IV), which is mainly due to the increase in the TT state energies (by about 0.2 eV on average, taking as reference the diabatic ground state $S_0S_0S_0$). Moreover, the $S_1^* - TT$ electronic couplings remain very small (<1 meV), although larger than in the Franck–Condon region ($t = 0$). We also see in Table IV that the $CT_1 \rightarrow S_0TT$ and $CT_1 \rightarrow TTS_0$ transitions occur with relatively large energy gaps (about 0.2 eV and 0.4 eV, respectively), which are however smaller than the ones at the initial geometries (about 0.7 eV), as a result of different lowerings of both the CT_1 and the TT energies, relative to $S_0S_0S_0$ (−1.0 eV for CT_1, −0.5 eV for S_0TT, and −0.7 eV for TTS_0). Such energy lowerings are mainly due to geometrical changes involving the relative position of the 3 QM molecules. As given in Table S14 at the $CT_1 \rightarrow S_0TT$ ($CT_1 \rightarrow TTS_0$) transitions, molecules B and C (or A and B) get closer to each other by about 0.17 (0.20) Å than at the starting time, with a decrease in the average distance, which is more pronounced for the two dihydrothiophene moieties than for the two pairs of fluorene groups. We also note (Tables S9 and S10) that at the $CT_1 \rightarrow S_0TT$ ($CT_1 \rightarrow TTS_0$) transition geometries, the CT_1 state is dominated by the $S_0B^+C^-$ ($A^+B^-S_0$) state, indicating that the mixing between the localized charge transfer states plays a minor role in its energy lowering. Furthermore, at these geometries, the $CT - TT$ electronic couplings tend to increase (see Table IV).

Overall, we see in Table III that the TT states are mainly populated by transitions from the S_2^* and S_1^* states, which predominate over the $CT \rightarrow TT$ transitions. In particular, the latter transitions occur at longer times (see Table IV and Fig. S5) and are associated with a smaller average net transition rate, during the whole simulation, than the $S_{1,2}^* \rightarrow TT$ ones (Table III). It appears that the population transfer through the CT states is here less important than their contribution to the $S_{1,2}^* - TT$ coupling, as highlighted by the effective Hamiltonian matrix elements: at the S_1^* hopping geometries, their averages are $\langle S_1^*|\hat{\mathscr{H}}_{eff}|S_0TT\rangle = -0.31 \pm 3.58$ meV and $\langle S_1^*|\hat{\mathscr{H}}_{eff}|TTS_0\rangle = -0.01 \pm 1.29$ meV, about three times their $\hat{\mathscr{H}}_{el}$ counterparts reported in Table IV (see Ref. 42 for the definition of the effective Hamiltonian).

In addition to S_0TT and TTS_0, the TTT state acquires a significant population, mainly by transitions from the CT_1 state (see Table S5). This is made possible, thanks to the considerable lower-

TABLE III. Average transition rates between pairs of states obtained in the nonadiabatic simulation of the excited state dynamics for a ThBF trimer embedded in its crystalline environment. The excitonic basis is considered. The charge transfer states, the delocalized excitonic states S_1^* and S_2^*, and the double triplet states are grouped together and indicated as CT, $S_{1,2}^*$, and TT, respectively. Each rate, defined as $\frac{\#\ transitions}{\#\ trajectories \cdot\ time\ interval}$, is computed over the whole simulation (time = 4 ps) and reported in units of ps^{-1}.

States		Rates (ps^{-1})		
i	j	$i \rightarrow j$	$j \rightarrow i$	net[a]
TT	$S_0S_0S_0$	0.000	0.000	0.000
$S_{1,2}^*$	$S_0S_0S_0$	0.019	0.019	0.000
S_3^*	$S_0S_0S_0$	0.002	0.000	0.002
TTT	$S_0S_0S_0$	0.000	0.000	0.000
CT	$S_0S_0S_0$	0.005	0.002	0.003
$S_{1,2}^*$	TT	0.476	0.341	0.135
S_3^*	TT	0.012	0.022	−0.010
TTT	TT	0.000	0.000	0.000
CT	TT	0.204	0.111	0.093
S_3^*	$S_{1,2}^*$	0.762	1.358	−0.596
TTT	$S_{1,2}^*$	0.043	0.046	−0.003
CT	$S_{1,2}^*$	7.320	6.587	0.733
TTT	S_3^*	0.002	0.007	−0.005
CT	S_3^*	4.043	4.877	−0.834
CT	TTT	0.046	0.031	0.015

[a]Difference between the $i \rightarrow j$ rate and the $j \rightarrow i$ one.

TABLE IV. Comparison of state energies and electronic couplings at the starting time (t = 0) and at the transitions between pairs of states ($i \rightarrow j$), averaged over all trajectories, obtained in the nonadiabatic simulation of the excited state dynamics for a ThBF trimer embedded in its crystalline environment. All energy differences and electronic couplings are reported in units of meV. For the electronic couplings, the standard deviation is also reported. X_0 indicates the initial geometry, and $X_{i\rightarrow j}$ indicates the hopping geometry.

States			Energies and coupling (meV)[a]				
i	j	Geom.	H_{ii}	H_{jj}	$(H_{jj}-H_{ii})$	H_{ij}	Time[b] (fs)
S_3^*	CT_1	X_0	2329.53	2388.09	58.55	−0.74 ± 6.77	0.0
		$X_{i\rightarrow j}$	2308.84	2302.42	−6.42	−2.90 ± 9.29	866.3
S_3^*	CT_2	X_0	2329.53	2477.36	147.83	−2.59 ± 6.42	0.0
		$X_{i\rightarrow j}$	2308.68	2319.36	10.68	−1.94 ± 7.45	1014.4
S_3^*	CT_3	X_0	2329.53	2572.39	242.86	−1.33 ± 6.44	0.0
		$X_{i\rightarrow j}$	2312.69	2339.74	27.05	−1.56 ± 8.28	1100.1
S_3^*	CT_4	X_0	2329.53	2685.46	355.93	−0.28 ± 5.76	0.0
		$X_{i\rightarrow j}$	2302.91	2346.88	43.97	−2.78 ± 6.04	1058.6
S_3^*	S_2^*	X_0	2329.53	2140.07	−189.46	0.00 ± 0.00	0.0
		$X_{i\rightarrow j}$	2293.85	2128.58	−165.27	0.00 ± 0.00	904.3
S_2^*	S_1^*	X_0	2140.07	1942.03	−198.04	0.00 ± 0.00	0.0
		$X_{i\rightarrow j}$	2110.61	1921.73	−188.88	0.00 ± 0.00	1040.2
CT_1	S_1^*	X_0	2388.09	1942.03	−446.06	5.99 ± 11.06	0.0
		$X_{i\rightarrow j}$	1878.25	1873.79	−4.46	2.21 ± 15.12	1325.4
CT_1	S_0TT	X_0	2388.09	1704.61	−683.47	−0.41 ± 7.94	0.0
		$X_{i\rightarrow j}$	1356.66	1170.75	−185.91	0.71 ± 21.22	1613.7
CT_1	TTS_0	X_0	2388.09	1710.27	−677.82	1.59 ± 7.00	0.0
		$X_{i\rightarrow j}$	1409.71	1021.49	−388.22	0.72 ± 12.22	1856.3
S_1^*	S_0TT	X_0	1942.03	1704.61	−237.42	−0.08 ± 0.12	0.0
		$X_{i\rightarrow j}$	1901.29	1890.80	−10.49	−0.14 ± 1.21	1534.1
S_1^*	TTS_0	X_0	1942.03	1710.27	−231.77	0.02 ± 0.13	0.0
		$X_{i\rightarrow j}$	1899.60	1911.57	11.97	0.00 ± 0.36	1753.7
CT_1	TTT	X_0	2388.09	2568.10	180.01	0.00 ± 0.00	0.0
		$X_{i\rightarrow j}$	1798.49	1702.39	−96.10	0.00 ± 0.01	1803.7

[a] H_{ii} and H_{jj} are the energies of states i and j, respectively, relative to the diabatic ground state, i.e., $S_0S_0S_0$, averaged over all transitions.
[b] Average time (in fs) for the initial or hopping geometries (X_0 or $X_{i\rightarrow j}$).

ing of the TTT energy that occurs when the monomers approach the adiabatic geometry of their T_1 states. Such a lowering is potentially three times the difference between the vertical and adiabatic transition energies of T_1, i.e., ~1.1.eV. At the time of the $CT_1 \rightarrow TTT$ hops, the lowering of the TTT energy averages to ~0.9 eV (see Table IV). On the contrary, the TS_0T state is never populated during 4 ps of simulation. Finally, we see that the ground state $S_0S_0S_0$ only gets a small population during the first 4 ps, mainly by transitions from the S_3^* and CT_1 states (Table S5). The reason is that the double triplet and TTT states, which are the most populated at the end of the simulation, are weakly coupled to the ground state and energetically well separated from it. For greater clarity, the aforementioned net fluxes of population are schematically illustrated in Fig. 7.

From the time evolution of the excitonic state populations (Fig. 6), we see a notable difference in the population of the two, apparently equivalent, TT states, the final population of S_0TT being about twice the one of TTS_0. This effect may be due to a drawback in the QM/MM ground state thermal equilibration, which is probably too short to account for the slow fluctuations needed to describe properly the symmetry of the QM subsystem, i.e., the equivalence of the two QM molecular pairs AB and BC. In particular, we see from Table S2 that the degeneracy condition is only nearly fulfilled by the two charge transfer state pairs $A^-B^+S_0/S_0B^+C^-$

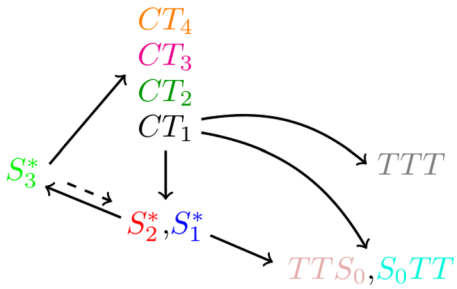

FIG. 7. Main net fluxes of population obtained from the nonadiabatic simulation of the excited state dynamics for a ThBF trimer embedded in its crystalline environment. A dashed arrow is used to indicate the initial transfer of population from S_3^* to S_2^* and S_1^*, which mainly occurs in the first 100 fs of simulation.

and $A^+B^-S_0/S_0B^-C^+$. As a result of this unsymmetrical situation, the $S_0B^+C^-$ state, which is most of the time the lowest charge transfer state in the thermal equilibration and the one associated with the largest transition dipole moment from $S_0S_0S_0$ (see Table II), mixes with the bright state S_3^* to a greater extent than the other charge transfer states, acquiring more population upon photoexcitation (see the initial populations of the diabatic states reported in Table S4). The differences in the populations of the charge transfer states become much more pronounced at later times, the $S_0B^+C^-$ state being by far the most populated charge transfer state after a few hundred fs (see Fig. S4). Therefore, transitions to S_0TT, the TT state that shows the largest electronic coupling with $S_0B^+C^-$ (see Table I and Tables S6–S13), are favored.

As mentioned above, we see in Fig. 6 that the TS_0T state, in which the two triplets are located on the second-nearest neighbor molecules A and C, is never populated in our simulation. This may be attributed to the very small matrix elements that couple TS_0T with both the excitonic and the charge transfer states included in our simulation (see Table I and Tables S6 to S12). Possible transitions to TS_0T are expected to occur at longer times, starting from the nearly degenerate S_0TT and TTS_0 states or from the higher TTT state.

Since the fluctuation amplitudes of the excitonic state populations are quite large at the end of the simulation, we evaluated the final populations by averaging over the last 100 fs (see Table S4). This way, the populations obtained for the $S_0S_0S_0$, TTS_0, S_0TT, and TTT long-lived states were 0.0234, 0.2956, 0.5501, and 0.0859, respectively. We extrapolated them to infinite time by assuming that the S_n^* and CT_n states would keep decaying to the above four states at rates proportional to those observed in average during the first 4 ps. The asymptotic populations of the long-lived states were then evaluated to be 0.024, 0.310, 0.576, and 0.090. Hence, the SF quantum yield (two triplet states for each TT state and three for TTT) turns out to be 2.04, which exceeds the theoretical maximum of 2 for a two-chromophore system.

V. COMPARISON WITH SIMULATIONS BASED ON A DIMER MODEL

To investigate how the delocalization over more than two molecules may influence the SF quantum yield and the transition rates, we performed a simulation of the same type, as described above (Sec. IV), but with only two molecules treated at the QM level, instead of three. A similar simulation was already presented in a previous paper by our group.[31] However, we repeated the dimer simulation in order to make it consistent in all details with the trimer one and allow for a meaningful comparison. The diabatization procedure, quite analogous to that used for the trimer, is shortly described in Sec. III and more in detail in Sec. S3.1.

A. Ground state thermal equilibration

In Fig. 8, we report the transition energies from S_0S_0 to the other five states in the excitonic basis, computed during the equilibration, as functions of time. Analogous data for the adiabatic and the localized diabatic states are found in Figs. S9 and S10. In Table V, we report the electronic Hamiltonian matrix in the excitonic basis, averaged over the last 10 ps of the thermal equilibration. More details and the Hamiltonian matrix in the diabatic basis are given in Table S15. We see that, as in the thermal equilibration for the trimer (Sec. IV A), the energies of the TT state (1.70 eV) and of the localized excitations S_1S_0 and S_0S_1 (~2.14 eV) are consistent with the vertical excitation energies of the isolated monomer. Moreover, the average excitation energies of the charge transfer states are close to those of the corresponding states in the trimer (see Table I and Table S2).

The main difference with respect to the trimer concerns the excitonic states S_1^* and S_2^*. Actually, the energies of the localized S_1S_0 and S_0S_1 states are very close to their trimer counterparts, and so is their mutual interaction (about 0.13 eV) if compared with the nearest neighbor interactions in the trimer (see Table S2). However, as predicted by the model with nearest neighbor interactions only (see Sec. S3.3), the average splitting $\overline{\Delta E}(S_1^* - S_2^*)$ in the dimer is smaller by a factor $\sim\sqrt{2}$ than $\overline{\Delta E}(S_1^* - S_3^*)$ in the trimer: 0.26 eV vs 0.39 eV. As a result, S_1^* lies about 0.07 eV higher in the dimer than in the trimer, leading to a larger $\overline{\Delta E}(TT - S_1^*)$: about 0.31 eV vs 0.23 eV. Even more important is the increase in the energy difference between the lowest CT state CT_1 and the highest S_n^* state (S_3^* for the trimer and S_2^* for the dimer). We see in Tables V and I that $\overline{\Delta E}(CT_1 - S_3^*) \simeq 0.05$ eV in the trimer, while $\overline{\Delta E}(CT_1 - S_2^*) \simeq 0.19$ in the dimer. Such a significant difference in the average energy gap is due to the combination of two effects: First, the already noted decrease in the average energy of the highest S_n^* state in going from the trimer to the dimer. Second, the presence of only two CT states in the dimer, instead of four as in the trimer, reduces the probability that at least one of these states gets lower (or higher) than a given energy value (see Sec. S3.4 for details). As a result of this statistical effect, in the dimer, the average transition energy for CT_1 is higher by about 0.08 eV than in the trimer.

On the other hand, the differences of the corresponding average electronic couplings are practically negligible in the two models. In particular, in the dimer, $\langle TT|\hat{\mathscr{H}}_{el}|S_1^*\rangle = -0.05 \pm 0.14$ meV and $\langle CT_1|\hat{\mathscr{H}}_{el}|S_2^*\rangle = 0.92 \pm 6.94$ meV (see Table S15), while in the trimer, $\langle S_0TT|\hat{\mathscr{H}}_{el}|S_1^*\rangle = -0.08 \pm 0.12$ meV, $\langle TTS_0|\hat{\mathscr{H}}_{el}|S_1^*\rangle = 0.04 \pm 0.12$ meV, and $\langle CT_1|\hat{\mathscr{H}}_{el}|S_3^*\rangle = -0.90 \pm 6.31$ meV (Table S2).

From the thermal equilibration of S_0^d (time interval of 4 ps–14 ps), we also computed the absorption spectrum shown in Fig. 9. We see that, as a result of the more limited exciton coupling in the dimer, the maximum of the most intense band of the spectrum (at

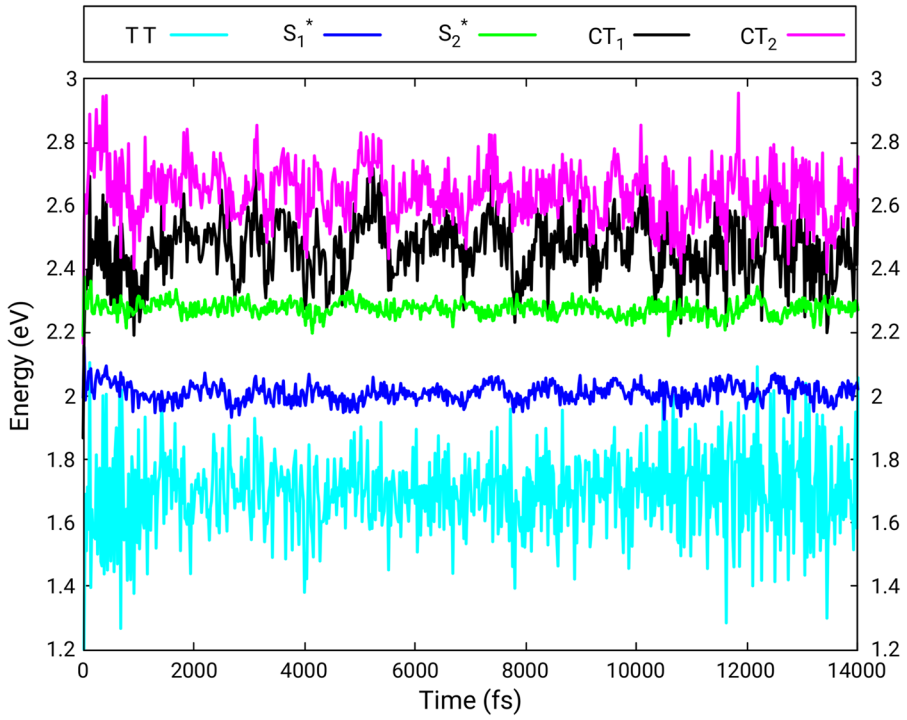

FIG. 8. Transition energies (in eV) from the ground state S_0S_0 to the other five excitonic states as functions of time, obtained from the ground state thermal equilibration for a ThBF dimer embedded in its crystalline environment. The reported results are obtained by averaging over time intervals of 20 fs.

~2.27 eV) is red-shifted by about 0.06 eV compared to the trimer (Fig. 5). Moreover, beside the S_3^d state, only S_4^d provides a significant contribution to the most intense band of the spectrum, while in the trimer, four adiabatic states are involved ($S_6^t - S_9^t$, see Fig. 5). This effect can be attributed to the more frequent energy switches of the CT states with the bright state S_3^* of the trimer, with respect to the analogous CT/S_2^* switches in the dimer, the difference being due to the respective energy gaps.

B. Simulation of excited state dynamics

From the set of phase points produced in the last 10 ps of the ground state thermal equilibration, 103 initial conditions were sampled with the procedure described in Refs. 38 and 39, using a transition energy window between 2.18 eV and 2.38 eV. As a result, 96 trajectories started in S_3^d, 6 in S_4^d, and 1 in S_2^d. The 6 low-lying adiabatic singlet states of the two QM molecules were included in the simulation.

TABLE V. Average electronic Hamiltonian matrix in the excitonic basis, obtained from the ground state thermal equilibration of a ThBF dimer embedded in its crystalline environment. For the off-diagonal elements, if twice the modulus of the mean value is lower than the standard deviation, the latter is reported and indicated with the symbol ±. All matrix elements are in units of meV. Time interval: 4 ps–14 ps. For more details, see Table S15.

$\hat{\mathscr{H}}_{el}$	S_0S_0	TT	S_1^*	S_2^*	CT_1	CT_2
S_0S_0	0.00	±0.09	±60.80	±70.61	±12.67	±10.68
TT	±0.09	1702.36	±0.14	±0.08	±10.02	±11.47
S_1^*	±60.80	±0.14	2010.74	0.00	9.77	9.85
S_2^*	±70.61	±0.08	0.00	2273.36	±6.94	±6.66
CT_1	±12.67	±10.02	9.77	±6.94	2463.54	0.00
CT_2	±10.68	±11.47	9.85	±6.66	0.00	2631.22

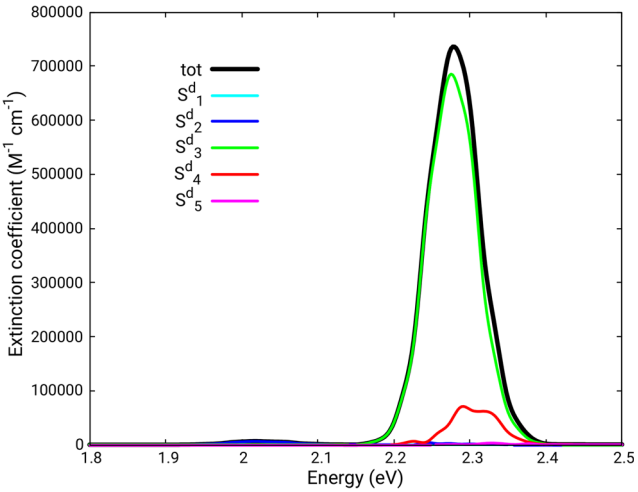

FIG. 9. Absorption spectrum obtained from the ground state thermal equilibration of a ThBF dimer embedded in its crystalline environment. Time interval: 4 ps–14 ps.

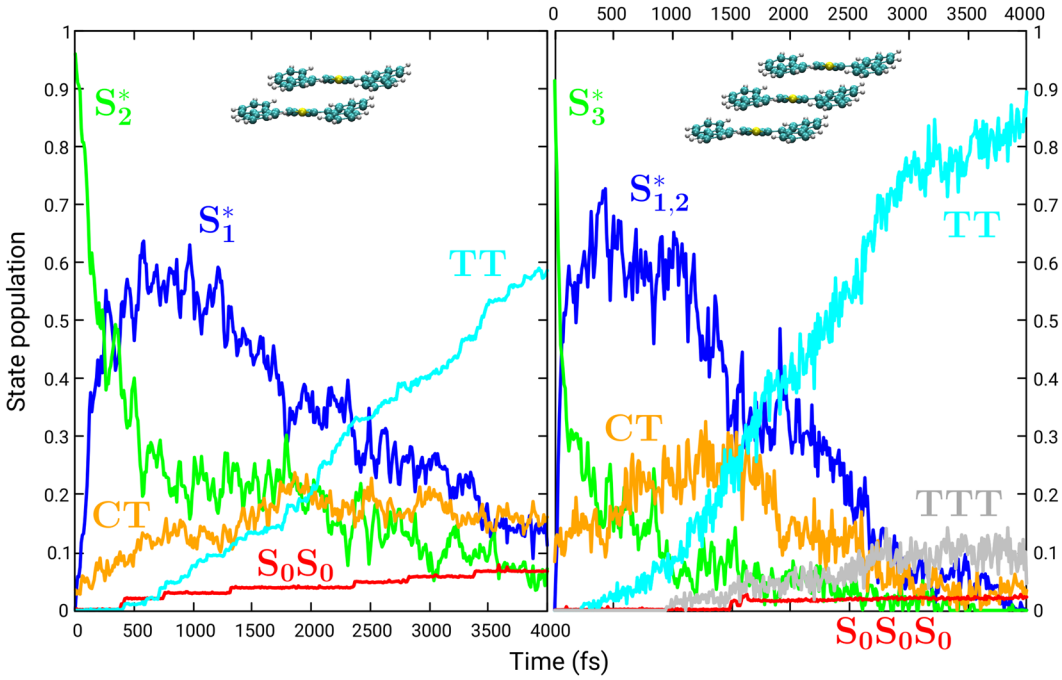

FIG. 10. State populations obtained in the simulations based on the dimer (left panel) and on the trimer (right panel) model. The charge transfer states, as well as the dark excitonic and the double triplet states for the trimer, are grouped together and indicated as *CT*, $S^*_{1,2}$, and *TT*, respectively.

In Fig. 10, we compare the excitonic state populations obtained with the dimer and the trimer models. To simplify the plots and highlight the essential features, we have grouped together the populations of the CT_n states in both models and, in trimer only, those of the S_1^* and S_2^* states, and those of the *TT* states. For more details on the dimer dynamics in the adiabatic, diabatic, and excitonic representations, see Figs. S12–S14. Moreover, in Table VI, we report the average transition rates between pairs of states along the whole simulation for the dimer model. Here too, the CT states are grouped together (for more details, see Table S19). In Fig. S15, we provide the net transition rates for selected pairs of states as functions of time, in the form of histograms. Finally, a schematic illustration of the net fluxes of population that take place during the simulation is shown in Fig. 11.

As shown in Fig. 10 and Fig. S15, starting from the initially most populated bright excitonic state S_2^*, transitions to both the dark state S_1^* and the CT states occur in the first few hundreds fs in the dimer as in the trimer simulations. However, the bright state to CT transfer of population is significantly slower in the dimer than in the trimer [see Figs. S5 and S15, panels (a)]. This effect is mainly due to the larger energy gaps that separate, in the dimer, the S_2^* state from the CT_n states at the starting geometries, as noted in Sec. V A. In fact, as in the trimer, transitions from the bright state S_2^* to the lowest charge transfer state CT_1 take place at geometries where the energy difference between states is very small (<0.01 eV), but in the dimer, a lowering of the CT_1 state such as to reach quasi-degeneracy with the bright state occurs more seldom than in the trimer. As in the trimer, these energy lowerings occur when the QM molecules get closer (see Tables S14 and S25). Moreover, the presence of fewer low lying CT states in the dimer (two vs four) contributes to slowing down the $S_2^* \rightarrow CT$ transfer of population (see Tables S5 and S19). Like in the trimer case, the $CT_2 \rightarrow CT_1$ transitions are very fast and the CT_2 state is scarcely populated.

TABLE VI. Average transition rates between pairs of excitonic states obtained in the nonadiabatic simulation of the excited state dynamics for a ThBF dimer embedded in its crystalline environment. The charge transfer states are grouped together and indicated as *CT*. Each rate, defined as $\frac{\#\ transitions}{\#\ trajectories\ \cdot\ time\ interval}$, is computed over the whole simulation (time interval = 4 ps) and reported in units of ps^{-1}.

States		Rates (ps^{-1})		
i	j	$i \rightarrow j$	$j \rightarrow i$	net[a]
TT	S_0S_0	0.000	0.000	0.000
S_1^*	S_0S_0	0.032	0.012	0.020
S_2^*	S_0S_0	0.012	0.017	−0.005
CT	S_0S_0	0.007	0.005	0.002
S_1^*	*TT*	0.371	0.318	0.053
S_2^*	*TT*	0.017	0.017	0.000
CT	*TT*	0.301	0.204	0.097
S_2^*	S_1^*	2.199	2.619	−0.420
CT	S_1^*	3.629	3.112	0.517
CT	S_2^*	3.272	3.930	−0.658

[a]Difference between the $i \rightarrow j$ rate and the $j \rightarrow i$ one.

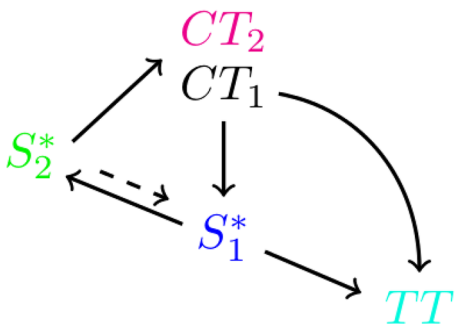

FIG. 11. Main net fluxes of population obtained from the nonadiabatic simulation of the excited state dynamics for a ThBF dimer embedded in its crystalline environment. A dashed arrow is used to indicate the initial transfer of population from S_2^* to S_1^*, which mainly occurs in the first 600 fs of simulation.

As a result of the slower increase in the CT_1 population in the dimer, both the $CT_1 \rightarrow S_1^*$ and $CT_1 \rightarrow TT$ transitions occur at significantly longer times in the dimer than in the trimer. This feature is enhanced by the larger energy lowering of CT_1 needed for such transitions in the dimer, ~1.3 eV vs ~1.0 eV for the trimer, taking as reference the ground state (see Tables IV and VII). Such energy lowerings are combined with a significant increase in the $CT_1 - TT$ coupling and, similar to the trimer, with a noticeable approach of the two QM molecules. The decrease in the average distances, compared to the starting geometries, is more pronounced for the two dihydrothiophene cores, ~0.29 Å, than for the two pairs of fluorene groups, ~0.13 and ~0.16 Å (see Table S25). Furthermore, we note an important slowdown in the $S_1^* \rightarrow TT$ transfer of population in the dimer [see Figs. S5 and S15, panel (d)], this effect being due not only to the slower $CT_1 \rightarrow S_1^*$ and $S_2^* \rightarrow S_1^*$ transitions (the latter compared to the $S_3^* \rightarrow S_{1,2}^*$ ones in the trimer) but also to the larger $S_1^* - TT$ initial energy gap, which must be overcome by lowering S_1^* (about −0.05 eV vs −0.04 eV in the trimer) and raising the TT state (about 0.24 eV vs 0.19 eV in the trimer) (see Tables IV and VII). Transitions from S_1^* also contribute significantly to the ground state population (see Table VI), which averages to ~0.07 during the last 100 fs. This value is about three times larger than the one obtained for the trimer (~0.02, see Tables S4 and S18).

We see in Table VI and Table S19 that, at variance with the simulations based on the trimer model, the TT state is mainly populated by transitions from the CT states (mostly from CT_1), which prevail over the $S_1^* \rightarrow TT$ transitions. The net rates of the two routes are 0.097 ps^{-1} and 0.053 ps^{-1}, respectively, while in the trimer we had 0.093 ps^{-1} and 0.135 ps^{-1} (Table III and Table S5). This change in the prevailing mechanism is essentially due to the higher $S_1^* \rightarrow TT$ transition rate in the trimer for the reasons seen above.

With the same assumptions as in Sec. IV B, i.e., that the S_n^* and the CT_n states keep decaying to TT and S_0S_0 proportionally to the average rates computed in the first 4 ps (see Table S18), we evaluate an asymptotic population for the TT state of 0.896. This corresponds to a SF quantum yield of 1.79, to be compared with 2.04 for the trimer (see Sec. IV B). This difference is partly due to the inability of the dimer model to account for the existence of the TTT state and

TABLE VII. Comparison of state energies and electronic couplings at the starting time (t = 0) and at the transitions between pairs of states ($i \rightarrow j$), averaged over all trajectories, obtained in the nonadiabatic simulation of the excited state dynamics for the ThBF dimer embedded in its crystalline environment. All energy differences and electronic couplings are reported in units of meV. For the electronic couplings, the standard deviation is also reported. X_0 indicates the initial geometry, and $X_{i\rightarrow j}$ indicates the hopping geometry.

States			Energies and coupling (meV)[a]				
i	j	Geom.	H_{ii}	H_{jj}	$(H_{jj}-H_{ii})$	H_{ij}	Time[b] (fs)
S_2^*	CT_1	X_0	2269.77	2476.28	206.51	−1.71 ± 7.30	0.0
		$X_{i\rightarrow j}$	2252.52	2261.61	9.09	−1.82 ± 9.46	1669.5
S_2^*	CT_2	X_0	2269.77	2644.48	374.71	0.78 ± 6.77	0.0
		$X_{i\rightarrow j}$	2260.66	2300.07	39.41	−1.51 ± 10.44	1831.5
S_2^*	S_1^*	X_0	2269.77	2012.94	−256.83	0.00 ± 0.00	0.0
		$X_{i\rightarrow j}$	2222.75	2021.85	−200.90	0.00 ± 0.00	1462.9
CT_1	S_1^*	X_0	2476.28	2012.94	−463.34	10.07 ± 7.46	0.0
		$X_{i\rightarrow j}$	1941.12	1932.96	−8.16	7.60 ± 15.09	1987.3
CT_1	TT	X_0	2476.28	1717.78	−758.51	0.25 ± 9.41	0.0
		$X_{i\rightarrow j}$	1168.17	1098.85	−69.32	16.45 ± 18.98	2587.6
S_1^*	TT	X_0	2012.94	1717.78	−295.17	−0.06 ± 0.16	0.0
		$X_{i\rightarrow j}$	1958.80	1953.89	−4.91	0.03 ± 0.50	1801.9

[a] H_{ii} and H_{jj} are the energies of states i and j, respectively, relative to the diabatic ground state, i.e., S_0S_0, averaged over all transitions.
[b] Average time (in fs) for the selected geometries (X).

to the slower transitions along the pathways that populate the *TT* state.

Overall, Fig. 10 shows that both the population and the depopulation of the CT states and of the dark S_1^* state (plus S_2^*, in the trimer) are faster in the trimer model than in the dimer one. In the attempt to extract the state lifetimes, we fitted the populations using a simple rate model (see Sec. S3.6 for details). From Fig. S16, we note that the selected rate model describes well the biexponential decay of the bright state in both cases, while it is unable to represent properly the population transfer from the excitonic states to the *TT* ones, especially in the trimer. Thus, to better compare the time evolutions of the state populations, we resorted to an *ad hoc* scheme. Namely, we estimated the decay time for the bright state, t_{decay}, as the time at which its population decreases to $P_0\ e^{-1}$, P_0 being its initial value. Moreover, for the (groups of) intermediate state(s), the CT ones and S_1^* ($S_{1,2}^*$), we took as reference the time at which the population reaches its maximum value, t_{max}. Finally, for the *TT* states, we defined the rise time, t_{rise}, as the time when the population gets equal to $P_\infty\ (1 - e^{-1})$, P_∞ being the asymptotic population. In this way, for the dimer (trimer), we obtained t_{decay} = 0.43 (0.10) ps for the bright state S_2^* (S_3^*), t_{max} = 0.58 (0.43) ps for the S_1^* ($S_{1,2}^*$) state(s), t_{max} = 1.86 (1.28) ps for the *CT* states, and t_{rise} = 3.80 (2.38) ps for the *TT* state(s). We see that all extracted times for the dimer are significantly longer than the corresponding ones for the trimer.

VI. CONCLUSIONS

We have presented and compared surface hopping simulations of singlet fission based on QM/MM schemes in which either two or three interacting QM molecules of 2,5-bis(fluorene-9-ylidene)-2,5-dihydrothiophene (ThBF) are embedded in their MM crystal environment. Our aim was to investigate the changes in the photodynamics that are brought about by extending the delocalization of the excited states beyond the minimal model of a dimer.

From our study, it turned out that in both models, dimer and trimer, the main steps of the singlet fission dynamics are the ultrafast decay of the bright excitonic state to both the dark state(s) and the charge transfer (CT) ones, the partial transfer of population from the CT to the lower lying dark state(s), and the final decay of all the previous states to populate the double triplet (*TT*) state(s). However, in the simulations based on the trimer model, compared to the dimer-based one, we have observed a faster time evolution of the state populations, with the largest differences associated with both the rise and decay times for the CT states. This effect was mainly attributed to the smaller average energy gaps between states in the trimer, while the electronic couplings were found to be about the same in the two models. Specifically, we found that the smaller energy difference between the initially populated bright state and the lowest CT state, as well as the closer proximity of the lowest dark state to the double triplets, plays the major roles in speeding up the dynamics in the trimer. Moreover, in the trimer-based simulations, we detected an appreciable population of the triple triplet state *TTT*, absent in the dimer, and a significantly smaller decay to the ground state. As a result, for the trimer, we predicted a singlet fission quantum yield of ~204%, which is larger than both the one extracted for the dimer (~179%) and the theoretical upper limit of 200% for the dimer-based model of singlet fission.

Of course, our model cannot account for the effects of extending the delocalization beyond three molecules, but our findings clearly indicate how and why the photodynamics can be affected. First of all, we confirm that delocalization can affect spectral properties, lifetimes, and quantum yields in singlet fission systems.[4,21–29] Therefore, the explicit consideration of more than two chromophores in dynamics simulations can be important. The more efficient population of the *TT* states we obtain by considering three instead of two chromophores is essentially due to the increased number of excitonic singlets, which are rapidly interconverted among them and extend on a broader energy range, bridging the gap between the CT and the *TT* states. Overall, these differences in the energetic aspects seem to be more important than the changes in the couplings between excitonic, *TT* and CT states. Our results emphasize the importance of geometry relaxation (both intra- and intermolecular) and thermal fluctuations in altering the relative energy levels. In this respect, other chromophores may behave differently: for instance, extended delocalization may be detrimental to singlet fission in systems where the exothermicity of the process is small [$\Delta E(S_1) \simeq 2\ \Delta E(T_1)$] and the packing is of J-type, instead of H-type.[43] A peculiarity of ThBF is the low adiabatic energy of T_1, which makes possible to populate the *TTT* state (the singlet combination of three triplets) in the trimer.

We also confirm the importance of the CT states[1–4,13–15,22–24] as intermediate steps in the decay of the bright state (especially for the trimer) but also as promoters of the superexchange coupling. We note that, if the CT states can be significantly populated, it is important to include them in the simulation, while the superexchange can be taken into account by a sufficiently accurate determination of the wavefunctions of the lower adiabatic states. The relative importance of the two mechanisms depends on the energy difference between the CT and the other states, which is in turn affected by delocalization. The involvement of low-lying CT states also points out that their energies should be accurately determined, by going beyond the mere assessment of the monomer energetics (see, for instance, Ref. 44).

SUPPLEMENTARY MATERIAL

The supplementary material includes a description of the QM/MM computational procedure (Sec. S1), details on the diabatization procedure and on the simulation results for the trimer model (Sec. S2), and analogous details concerning the dimer model and the comparison between the two models (Sec. S3).

ACKNOWLEDGMENTS

This work was partly performed in the framework and with funds of the ITN-EJD-642294-TCCM project and was also funded by the University of Pisa (Grant No. PRA 2018 36).

DATA AVAILABILITY

The data that supports the findings of this study are available within this article and its supplementary material.

REFERENCES

[1] M. B. Smith and J. Michl, "Singlet fission," Chem. Rev. **110**, 6891–6936 (2010).
[2] M. B. Smith and J. Michl, "Recent advances in singlet fission," Annu. Rev. Phys. Chem. **64**, 361–386 (2013).
[3] A. Japahuge and T. Zeng, "Theoretical studies of singlet fission: Searching for materials and exploring mechanisms," ChemPlusChem **83**, 146–182 (2018).
[4] D. Casanova, "Theoretical modeling of singlet fission," Chem. Rev. **118**, 7164–7207 (2018).
[5] V. K. Thorsmølle, R. D. Averitt, J. Demsar, D. L. Smith, S. Tretiak, R. L. Martin, X. Chi, B. K. Crone, A. P. Ramirez, and A. J. Taylor, "Morphology effectively controls singlet-triplet exciton relaxation and charge transport in organic semiconductors," Phys. Rev. Lett. **102**, 017401–017404 (2009).
[6] J. J. Burdett, A. M. Müller, D. Gosztola, and C. J. Bardeen, "Excited state dynamics in solid and monomeric tetracene: The roles of superradiance and exciton fission," J. Chem. Phys. **133**, 144506 (2010).
[7] M. W. B. Wilson, A. Rao, J. Clark, R. S. S. Kumar, D. Brida, G. Cerullo, and R. H. Friend, "Ultrafast dynamics of exciton fission in polycrystalline pentacene," J. Am. Chem. Soc. **133**, 11830–11833 (2011).
[8] J. Lee, P. Jadhav, P. D. Reusswig, S. R. Yost, N. J. Thompson, D. N. Congreve, E. Hontz, T. Van Voorhis, and M. A. Baldo, "Singlet exciton fission photovoltaics," Acc. Chem. Res. **46**, 1300–1311 (2013).
[9] W. Shockley and H. J. Queisser, "Detailed balance limit of efficiency of p-n junction solar cells," J. Appl. Phys. **32**, 510–519 (1961).
[10] M. C. Hanna and A. J. Nozik, "Solar conversion efficiency of photovoltaic and photoelectrolysis cells with carrier multiplication absorbers," J. Appl. Phys. **100**, 1–8 (2006).
[11] R. Nagata, H. Nakanotani, W. J. Potscavage, Jr., and C. Adachi, "Exploiting singlet fission in organic light-emitting diodes," Adv. Mater. **30**, 1801484 (2018).
[12] L. R. Weiss, S. L. Bayliss, F. Kraffert, K. J. Thorley, J. E. Anthony, R. Bittl, R. H. Friend, A. Rao, N. C. Greenham, and J. Behrends, "Strongly exchange-coupled triplet pairs in an organic semiconductor," Nat. Phys. **13**, 176–181 (2017).
[13] N. Monahan and X.-Y. Zhu, "Charge transfer-mediated singlet fission," Annu. Rev. Phys. Chem. **66**, 601–618 (2015).
[14] W.-L. Chan, T. C. Berkelbach, M. R. Provorse, N. R. Monahan, J. R. Tritsch, M. S. Hybertsen, D. R. Reichman, J. Gao, and X.-Y. Zhu, "The quantum coherent mechanism for singlet fission: Experiment and theory," Acc. Chem. Res. **46**, 1321–1329 (2013).
[15] T. C. Berkelbach, M. S. Hybertsen, and D. R. Reichman, "Microscopic theory of singlet exciton fission. II. Application to pentacene dimers and the role of superexchange," J. Chem. Phys. **138**, 114103 (2013).
[16] T. Zeng, R. Hoffmann, and N. Ananth, "The low-lying electronic states of pentacene and their roles in singlet fission," J. Am. Chem. Soc. **136**, 5755–5764 (2014).
[17] X. Feng, A. B. Kolomeisky, and A. I. Krylov, "Dissecting the effect of morphology on the rates of singlet fission: Insights from theory," J. Phys. Chem. C **118**, 19608–19617 (2014).
[18] L. Wang, Y. Olivier, O. V. Prezhdo, and D. Beljonne, "Maximizing singlet fission by intermolecular packing," J. Phys. Chem. Lett. **5**, 3345–3353 (2014).
[19] E. A. Buchanan, Z. Havlas, and J. Michl, "Singlet fission: Optimization of chromophore dimer geometry," Adv. Quantum Chem. **75**, 175–227 (2017).
[20] M. H. Farag and A. I. Krylov, "Singlet fission in perylenediimide dimers," J. Phys. Chem. C **122**, 25753–25763 (2018).
[21] E. A. Buchanan and J. Michl, "Optimal arrangements of 1,3-diphenylisobenzofuran molecule pairs for fast singlet fission," Photochem. Photobiol. Sci. **18**, 2112–2124 (2019).
[22] N. J. Hestand, H. Yamagata, B. Xu, D. Sun, Y. Zhong, A. R. Harutyunyan, G. Chen, H.-L. Dai, Y. Rao, and F. C. Spano, "Polarized absorption in crystalline pentacene: Theory vs experiment," J. Phys. Chem. C **119**, 22137–22147 (2015).
[23] S. Sharifzadeh, C. Y. Wong, H. Wu, B. L. Cotts, L. Kronik, N. S. Ginsberg, and J. B. Neaton, "Relating the physical structure and optoelectronic function of crystalline tips-pentacene," Phys. Rev. B **25**, 2038–2046 (2015).
[24] T. C. Berkelbach, M. S. Hybertsen, and D. R. Reichman, "Microscopic theory of singlet exciton fission. III. Crystalline pentacene," J. Chem. Phys. **141**, 074705 (2014).
[25] H. Tamura, M. Huix-Rotllant, I. Burghardt, Y. Olivier, and D. Beljonne, "First-principles quantum dynamics of singlet fission: Coherent versus thermally activated mechanisms governed by molecular π stacking," Phys. Rev. Lett. **115**, 107401 (2015).
[26] P. E. Teichen and J. D. Eaves, "Collective aspects of singlet fission in molecular crystals," J. Chem. Phys. **143**, 044118 (2015).
[27] M. Nakano, T. Nagami, T. Tonami, K. Okada, S. Ito, R. Kishi, Y. Kitagawa, and T. Kubo, "Quantum master equation approach to singlet fission dynamics in pentacene linear aggregate models: Size dependences of excitonic coupling effects," J. Comput. Chem. **40**, 89–104 (2019).
[28] R. D. Pensack, A. J. Tilley, S. R. Parkin, T. S. Lee, M. M. Payne, D. Gao, A. A. Jahnke, D. G. Oblinsky, P.-F. Li, J. E. Anthony, D. S. Seferos, and G. D. Scholes, "Exciton delocalization drives rapid singlet fission in nanoparticles of acene derivatives," J. Am. Chem. Soc. **137**, 6790–6803 (2015).
[29] S. T. Roberts, R. E. McAnally, J. N. Mastron, D. H. Webber, M. T. Whited, R. L. Brutchey, M. E. Thompson, and S. E. Bradforth, "Efficient singlet fission discovered in a disordered acene film," J. Am. Chem. Soc. **134**, 6388–6400 (2012).
[30] S. Kawata, Y.-J. Pu, A. Saito, Y. Kurashige, T. Beppu, H. Katagiri, M. Hada, and J. Kido, "Singlet fission of non-polycyclic aromatic molecules in organic photovoltaics," Adv. Mater. **28**, 1585–1590 (2016).
[31] M. Wibowo, M. Persico, and G. Granucci, "Nonadiabatic dynamics simulations of singlet fission in 2,5-bis(fluorene-9-ylidene)-2,5-dihydrothiophene crystals," Phys. Chem. Chem. Phys. **21**, 692–701 (2019).
[32] D. Accomasso, G. Granucci, R. W. A. Havenith, and M. Persico, "Testing new chromophores for singlet fission: A computational protocol applied to 2,3-diamino-1,4-benzoquinone," Chem. Phys. **515**, 635–642 (2018).
[33] H. J. C. Berendsen, J. P. M. Postma, W. F. van Gunsteren, A. DiNola, and J. R. Haak, "Molecular dynamics with coupling to an external bath," J. Chem. Phys. **81**, 3684–3690 (1984).
[34] J. W. Ponder, TINKER—Software tools for molecular design, Version 6.3, Copyright (c), 2014.
[35] G. Granucci, M. Persico, and A. Toniolo, "Direct semiclassical simulation of photochemical processes with semiempirical wave functions," J. Chem. Phys. **114**, 10608–10615 (2001).
[36] J. J. P. Stewart, "Optimization of parameters for semiempirical methods II. Applications," J. Comput. Chem. **10**, 221–264 (1989).
[37] G. Bussi and M. Parrinello, "Stochastic thermostats: Comparison of local and global schemes," Comput. Phys. Commun. **179**, 26–29 (2008).
[38] L. Creatini, T. Cusati, G. Granucci, and M. Persico, "Photodynamics of azobenzene in a hindering environment," Chem. Phys. **347**, 492–502 (2008).
[39] M. Persico and G. Granucci, "An overview of nonadiabatic dynamics simulations methods, with focus on the direct approach versus the fitting of potential energy surfaces," Theor. Chem. Acc. **133**, 1526-1–1526-28 (2014).
[40] M. Persico, G. Granucci, S. Inglese, T. Laino, and A. Toniolo, "Semiclassical simulation of photochemical reactions in condensed phase," J. Mol. Struct. THEOCHEM **621**, 119–126 (2003).
[41] G. Granucci, M. Persico, and A. Zoccante, "Including quantum decoherence in surface hopping," J. Chem. Phys. **133**, 134111-1–134111-9 (2010).
[42] D. Accomasso, M. Persico, and G. Granucci, "Diabatization by localization in the framework of configuration interaction based on floating occupation molecular orbitals (FOMO-CI)," ChemPhotoChem. **3**, 933–944 (2019).
[43] F. C. Spano, "The spectral signatures of Frenkel polarons in h- and j-aggregates," Acc. Chem. Res. **43**, 429–439 (2010).
[44] P. B. Coto, S. Sharifzadeh, J. B. Neaton, and M. Thoss, "Low-lying electronic excited states of pentacene oligomers: A comparative electronic structure study in the context of singlet fission," J. Chem. Theory Comput. **11**, 147–156 (2010).